Evaluation of a Laser-Dot Grid-Projection System for Lunar Lander Crater-Shape and Ejecta-Sheet Measurements

Joshua M. Weisberger*, Olivia K. Tyrrell†, Paul M. Danehy‡, and Timothy W. Fahringer§
NASA Langley Research Center, Hampton, VA, 23681

Development, testing, and evaluation of an active-illumination laser-dot grid-projection system was performed to evaluate its potential inclusion on an upcoming uncrewed lunar lander mission to the south pole region of the moon. Active illumination may be required for this mission due to the shallow angle of the sun at the landing location, which may cast shadows in the landing region, hindering the stereo camera imaging system's ability to determine the pre- and post-landing lunar surface/crater shape. Testing includes characterization of the diffractive optical elements used for the grid projection, single-camera tests to determine the imaged laser dot intensity as a function of camera exposure and imaging angle relative to the laser grid projection, laser dot brightness/saturation impact on depth map calculations, angle of imaged laser grid impact on depth map calculations for steep crater edges, impact of density gradients on the depth map calculations, and the feasibility of making measurements of the ejecta sheet.

I. Introduction

The entry, descent, and landing (EDL) phases of a lunar lander are critical for the overall success of the mission. During these phases, the rocket plume impinges on the lunar surface below, forming a crater as lunar regolith is ejected from below the lander at high velocities in all directions. This process has the potential to damage the lander and nearby existing equipment/structures [1–8]. Computer simulations of the plume-surface interaction (PSI) process require measurements for validation. While testing of some aspects of this PSI phenomenon can be performed in laboratories or specialized ground test facilities [9–11], no testing can entirely replicate exact lunar conditions. Due to these limitations, dedicated instrumentation to study PSI is being developed for several uncrewed lunar lander missions that are planned for the Commercial Lunar Payload Services (CLPS) initiative. One of the instruments to be flown is the Stereo Cameras for Lunar-Plume Surface Studies (SCALPSS), which aims to measure the lunar surface before, during, and after landing using cameras arranged in a stereo-imaging configuration, and will provide images that can be used to calculate the change in shape of the resulting crater during landing [12, 13].

While the SCALPSS imaging system can acquire images when the surface is fully illuminated by the sun, a landing at the lunar south pole may result in portions of the landing area and lander-generated crater that are shadowed due to the shallow angle of the sun. Crater-shape measurements in these shadowed regions will not be possible without active illumination. One such proposed active illumination method is to project a grid of laser dots onto the lunar surface using a diffractive optical element (DOE). Recent studies have evaluated this concept for an upcoming CLPS mission [14, 15], but further testing is required before finalizing the camera operating parameters, laser power, and DOE design, to ensure a successful measurement with high-quality data. These decisions can be broken into operating/design parameters and into engineering/implementation considerations. The operating/design parameters will be discussed in this paper (laser power, number of laser dots from DOE, camera exposure/gain), while the engineering/implementation work is ongoing, and can only be fully completed after the design decisions have been made.

Several tests were conducted to further evaluate the feasibility of the laser-dot grid projection for use with the SCALPSS system on a lunar lander, including verification of the DOE divergence angles and dot power distribution (Section II), the dependence on imaged dot intensity with camera viewing angle relative to the laser (Section III), the impact of laser dot image brightness and saturation on the computed depth map (Section IV), the impact of a highly angled camera view of the laser grid on the computed depth map (Section V), the feasibility of making measurements of the ejecta sheet (Section VI), and the impact of non-uniform density gradients on the computed depth map (Section VII).

*Research Engineer, Advanced Measurements and Data Systems Branch, AIAA Senior Member.
†Research Engineer, Advanced Measurements and Data Systems Branch, AIAA Member.
‡Senior Technologist, Advanced Measurements and Data Systems Branch, AIAA Associate Fellow.
§Research Engineer, Advanced Measurements and Data Systems Branch.

II. Diffractive Optical Element Characterization

All the DOEs used for testing in this paper were purchased off-the-shelf from a catalog of existing elements. To evaluate the concept and reduce testing cost and time, plastic DOE elements were selected, with a range of operating wavelengths (λ), grid pattern divergence angles (β), and number of grid dots ($N \times N$). The testing performed in this paper will lead to the selection of an optimum DOE for a future SCALPSS mission, which can then be manufactured specifically to the desired design requirements. While it should be anticipated that the datasheets accompanying the DOEs are accurate in their performance characteristics, the testing in this section was performed to verify these values.

The light from a diode-pumped solid-state laser emitting at $\lambda = 638$ nm (RPMC Lasers, Inc.) was transmitted through the DOE to produce a grid of laser dots. These DOEs were small and lightweight, making them an attractive option for laser beam splitting for a lunar lander, where size and weight are important considerations. For this free-space laser, the power can be set at any value up to its maximum of 600 mW, and because the output beam diverges in the horizontal direction, a cylindrical lens ($f = 150$ mm) was used to roughly collimate the light to an optimum beam size for the DOEs (typically a diameter of 2-3 mm as provided in the manufacturer's datasheet). To evaluate the wavelength-dependence of the projection characteristics, two low-power (≈ 0.9 mW) lasers were also used, one emitting at $\lambda = 520$ nm (Thorlabs, PL201) and the other at $\lambda = 405$ nm (Thorlabs, PL205), both with beam diameters of approximately 3 mm.

Example images of both a 21×21 and a 17×17 laser dot grid projection are shown in Figs. 1a and 1b, respectively, where the image of Fig. 1a was taken with a phone camera and the image of Fig. 1b was taken with a machine vision camera. The engineered diffractive surface of the DOE split the single incident beam into an array of separate beams, the shape/size of which depended both on the design of the DOE surface structure and the wavelength/diameter of the incident laser light beam. In Fig. 1a, a bright 0^{th}-order dot is visible along with an array of weaker 1^{st}-order dots. The brightness of the central 0^{th}-order dot typically depends on the difference between the laser wavelength and the DOE design wavelength; the closer the laser wavelength is to the design wavelength, the closer the intensity of the 0^{th}-order dot to the 1^{st}-order dots. For example, in Fig. 1a, a 520 nm laser was incident on a DOE designed for 635 nm, and thus a relatively bright 0^{th}-order dot is visible. In contrast, in the image of Fig. 1b (DOE designed for 635 nm and illuminated with 638 nm), no 0^{th}-order dot is visible, and the 1^{st}-order dot grid is of nominally uniform intensity over all the dots. However, higher-order dots outside the designed 17×17 grid are visible. In the images of Fig. 1, power is distributed to the 0^{th}-order and higher order dots, respectively, removing power from the desired 1^{st}-order dots used for the crater shape measurements.

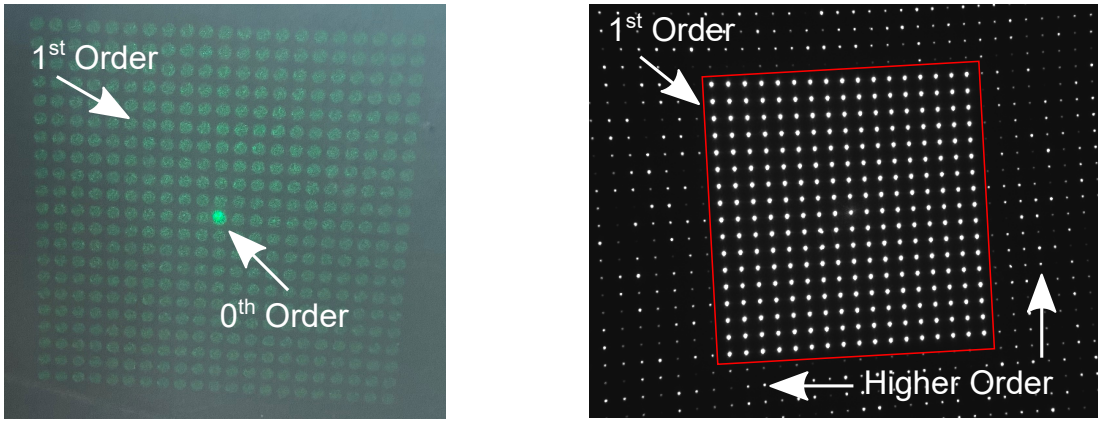

(a) **(b)**

Fig. 1 (a) Phone camera image of a 21×21 DOE designed for 635 nm and illuminated with 520 nm, and (b) machine vision camera image of a 17×17 DOE designed for 635 nm and illuminated with 638 nm.

The DOEs were evaluated to determine their maximum divergence angle (how much the grid spreads out over a given distance) and the laser power distribution in the projected dots. These measurements will be used to develop a design tool to aid selection of the DOE for the stereo imaging camera system. Such a system will be optimized for the altitude of the cameras, expected overlapping stereo field-of-view, required grid dot intensity for laser power and

camera exposure, etc. The main DOEs tested here are square grids of 11×11, 17×17, 21×21, 51×51, and 101×101 dots. Most of these DOEs are optimized for roughly 630 - 660 nm, although two duplicate DOEs that are optimized for roughly 520 - 532 nm were tested as well (21×21, 51×51). Testing was performed by projecting the collimated laser beam through the DOE and onto a flat surface, orthogonal to the central axis of the laser beam, at three fixed distances away from the DOE (63 cm, 94 cm, 124 cm). The distance between the outermost dots of the grid in both the vertical and horizontal direction were measured, and the divergence angle computed using these values and the known distance from the DOE to the flat surface.

Table 1 Comparison of measured DOE divergence angle with manufacturer's datasheet. All measured values are averaged over six measurements: horizontal and vertical divergence angle at three DOE distances from the flat surface.

Part Number	Grid Pattern	$\lambda_{\text{datasheet}}$	$\lambda_{\text{measured}}$	$\beta_{\text{datasheet}}$	β_{measured}
DE-R 258	11×11	635 nm	638 nm	28.2°	29.5°
			405 nm		17.7°
			520 nm		23.1°
DE-R 243	17×17	635 nm	638 nm	5.0°	5.1°
			405 nm		3.2°
			520 nm		4.1°
DE-R 206	17×17	660 nm	638 nm	15.2°	14.9°
			405 nm		9.3°
			520 nm		11.9°
DE-R 241	21×21	635 nm	638 nm	4.8°	4.8°
			405 nm		3.1°
			520 nm		3.9°
DE-R 389	21×21	520 nm	520 nm	18.8°	18.9°
			405 nm		14.7°
			638 nm		24.0°
DE-R 257	51×51	660 nm	638 nm	22.8°	22.6°
			405 nm		13.9°
			520 nm		17.8°
DE-R 388	51×51	532 nm	520 nm	18.8°	18.6°
			405 nm		14.3°
			635 nm		23.3°
DE-R 231	101×101	660 nm	638 nm	5.2°	5.1°
			405 nm		3.2°
			520 nm		4.1°

Table 1 contains the results of the divergence measurements for all tested DOEs, with comparisons to the manufacturer's datasheet values. Measurements with three laser wavelengths are provided for each DOE, which are an average of all horizontal and vertical divergences angles calculated (six total: horizontal and vertical for three positions). The standard deviation of the six computed divergence angles for all DOEs was roughly 0.1°. For each DOE, the differences between the design and measured divergence angles at the design wavelength are reasonably small, while the measurements taken with the lasers not matching the design wavelength of the DOE can be used to determine the divergence angle as a function of wavelength.

The power distributions of the dot patterns were measured next. A 16% transmission power loss was measured through the cylindrical collimation lens due to the absence of an anti-reflection coating. For each DOE, power measurements were made of the bright central dot (0^{th}-order) and the outer 1^{st}-order grid dots. The higher-order dots located outside the main 1^{st}-order grid were not measured. The total power of the usable grid dots was then calculated

by multiplying the 1st-order dot power (P_1) by the total number of dots (D) minus one (i.e., excluding the 0th-order dot). The power ratio was computed using this measured data divided by the incident power to the DOE.

$$P_{\text{measured}} = (D-1)\,P_1 \qquad \text{and} \qquad P_{\text{ratio}} = \frac{P_{\text{measured}}}{P_{\text{incident}}} \tag{1}$$

The reason for excluding the 0th-order dot power from this calculation is that its intensity can overshadow the power of the 1st-order dots used for the crater shape measurement, and the camera exposure is set to correctly expose only the 1st-order dots.

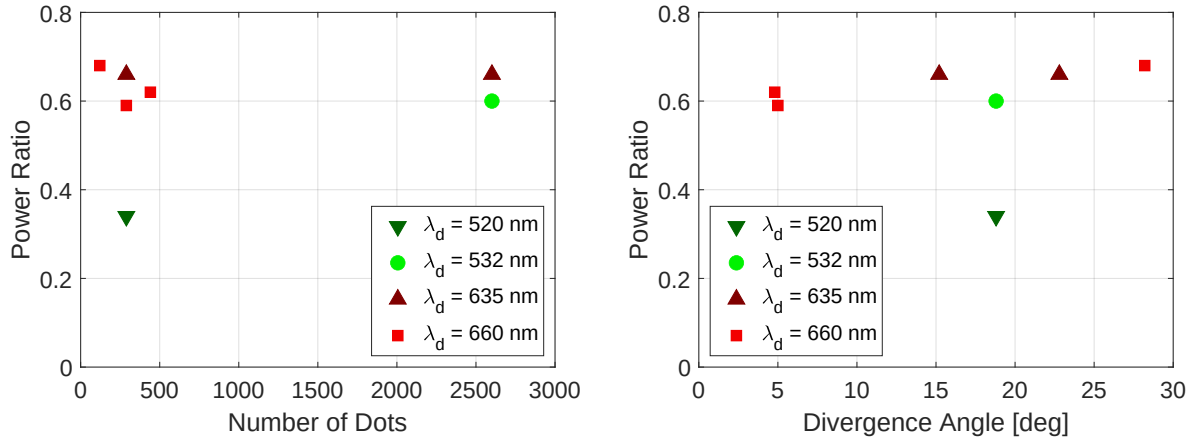

Fig. 2 Power ratio of the projected dots versus (a) number of dots in grid pattern and (b) divergence angle of grid pattern, using a laser wavelength of 638 nm. Colored markers roughly correspond to the design wavelength of the DOE.

The power ratio is plotted as a function of the total number of grid dots in Fig. 2a, and as a function of the DOE divergence angle in Fig. 2b, where the colors roughly correspond to the design wavelength of the DOE, although note that the illumination source was always the 638 nm laser. In both plots, the power ratio of all the data is roughly between 0.6 and 0.7, aside from the DOE at a design wavelength of 520 nm (green inverted triangle), due to a very bright 0th-order dot. Interestingly, the 0th-order dot for the DOE at the design wavelength of 532 nm was not as bright (green circle). For all the other DOEs tested, the number of dots, divergence angle, and the design wavelength do not appear to have an influence on the power ratio of the projected grids. That is, the total power from the laser that is converted into the primary grid to be imaged by the camera system is roughly the same for all DOEs, and the same amount of power is lost to the combination of 0th-order and higher-order diffraction dots. While these plots do not show the distribution between the 0th-order and higher-order dots for each, the important design value is what amount of incident laser power is converted to useful 1st-order dot power.

III. Lunar Regolith Simulant Testing

A. Experimental Setup and Data Processing

Tests were performed to evaluate the relationship between the imaged laser dot intensities as a function of angle between the camera's optical axis and the laser grid projection axis. Four target materials were tested to evaluate how each reflected and scattered the laser light toward the camera. Two lunar regolith simulants were tested, which were developed to possess similar mechanical properties to lunar dust. The first, LHS-1 Lunar Highlands Simulant, simulates an average highlands location on the moon such as that expected at the south pole, while the second, LMS-1 Lunar Mare Simulant, simulates an average mare region such as that expected at an equatorial landing site. Both simulants

have a particle size distribution that is targeted to match that of typical Apollo soils. Details of both simulants can be found in the database of the University of Central Florida Center for Lunar and Asteroid Surface Science (CLASS) [16, 17]. A piece of white foam board and a piece of retroreflective film (3M™ Scotchlite 7610) were also tested as target materials to provide a comparison for the regolith simulants. The reason for including the retroreflective material is that the lunar regolith has been noted to have a slight retroreflective optical property. However, it is not expected that the regolith simulants used here, LMS-1 and LHS-1, will have any retroreflective optical properties since they are designed to simulate the lunar regolith both in size/shape of the particles and in the composition (mechanical properties), but not necessarily the optical properties.

For these tests, a stereo imaging system was not required, so only a single camera was used, mounted to an aluminum rail which was connected to a rotating hinge directly below the laser/DOE, as shown in the side-view schematic of Fig. 3a. By rotating this rail, the angle between the camera optical axis and the laser/DOE grid axis could be changed without changing the imaging distance. The angle θ was measured between the laser/DOE axis and the camera optical axis, such that an angle of 0° corresponded to parallel axes. For simulant testing, a tray with an approximately 10 mm thick layer of either LHS-1 or LMS-1 was placed directly below the laser, and positioned such that the grid just filled the extents of the tray, as shown in the image of Fig. 3b for LHS-1. The tray used for LMS-1 was slightly smaller, and so only 15 of the total 17 rows of laser dots were incident on the LMS-1 simulant. When the white foam board or retroreflective material was used as the target, the simulant trays were removed and the appropriate target material was placed below the laser/DOE such that all the grid points were incident on the target. The measured heights, h, were 144 cm, 138 cm, 128 cm, 106 cm, and 91 cm, roughly corresponding to angles of θ = 0°, 16°, 28°, 43°, and 51°, respectively (±2° due to measurement uncertainties).

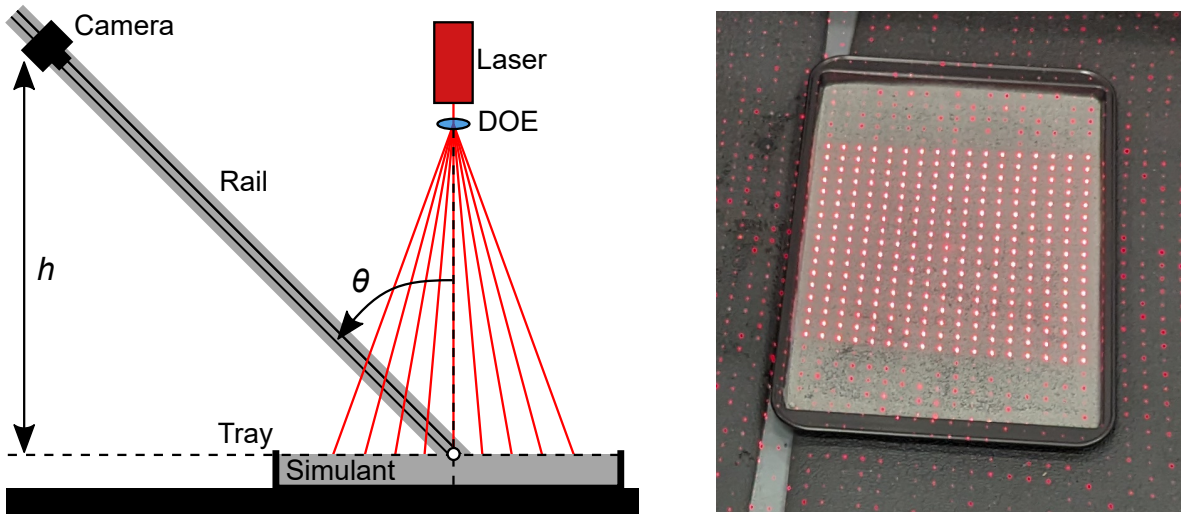

(a) (b)

Fig. 3 (a) Side-view schematic of the camera and laser system used for static regolith testing and (b) close-up picture of the 17×17 laser-dot grid projection on the LHS-1 lunar simulant in the tray, imaged with a phone camera.

The room lights were turned off so that the only light incident on the camera sensor was the reflected/scattered light from the target material. By positioning the camera optical axis parallel with the aluminum rail, at each rotation angle, the center of the projected laser grid remained at the center of the camera's image as verified by a central cross-hair target in the camera software. For each camera angle θ, images over a range of exposures were acquired. All data for a single target material was taken before switching to the next target material to ensure the material did not move between tests. During testing with a single target material, the angle was set to a specific θ and all exposure images were taken. This was repeated for each angle, after which the target material was changed, and the same procedure used until all data were acquired. The data processing for the images proceeds by finding the peak pixel value for each laser dot in the image, and averaging these pixel values over all laser dots to return a single peak laser dot intensity for each image (called the peak spot intensity in later plots). For the LHS-1, white foam board, and retroreflective material targets, 289

laser dots are identified and averaged, whereas only 255 laser dots are used for the LMS-1 target due to the smaller tray size mentioned earlier.

B. Exposure, Angle, and Target Material Dependence

Raw images taken with a laser power of 100 mW for the LMS-1 simulant are shown in Fig. 4, where Fig. 4a includes images at a viewing angle of 62° for varying camera exposures (not showing all acquired exposure images), and Fig. 4b includes images at an exposure of 5 ms for all five viewing angles. All images have been cropped to only include the laser grid for clarity. As the exposure increases in Fig. 4a, the intensity of the images' laser dots increases, and the dot intensities over the entire grid are uniform. As the imaging angle decreases towards a more normal imaging angle in Fig. 4b, the overall intensity of the laser dots increases, although the effect is not very pronounced in the images.

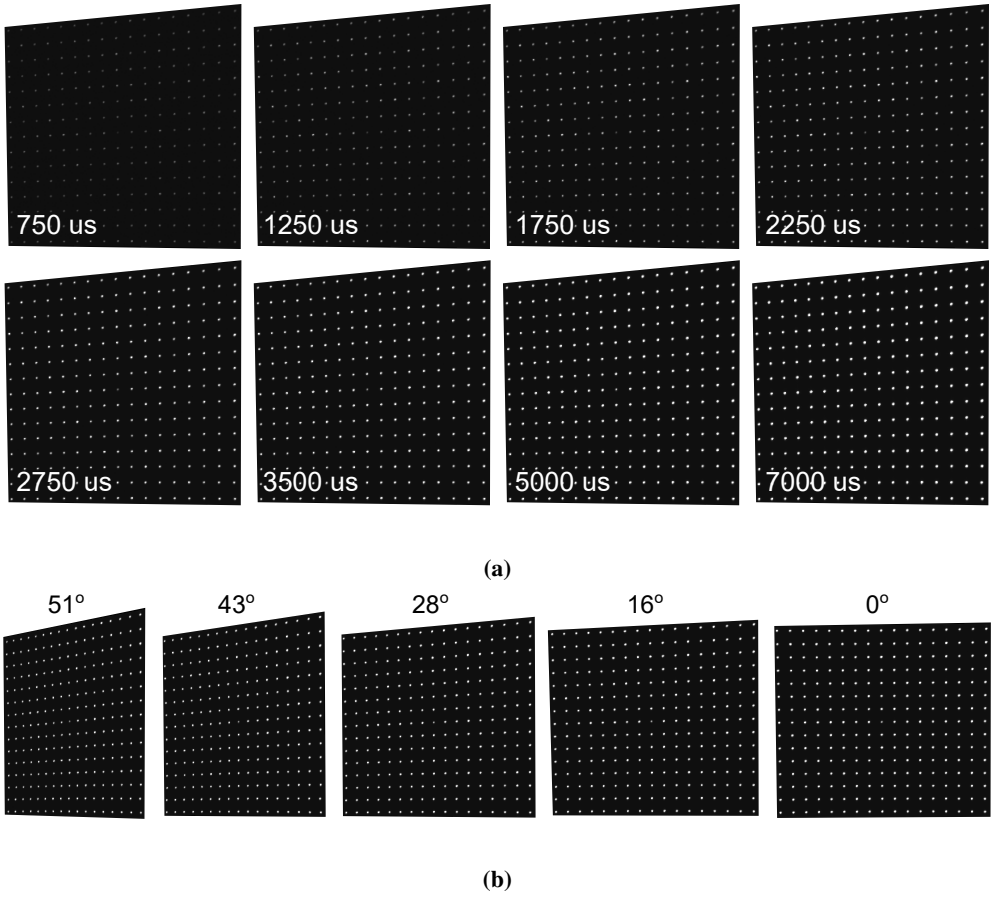

Fig. 4 Raw (cropped) images of laser grid projecting onto LMS-1 simulant at (a) varying exposures and (b) varying imaging angle.

The effect of changing both exposure and imaging angle can be more clearly seen in the plot of Fig. 5 for all four materials tested, where the images have been processed as described in Section III.A to obtain a peak spot intensity for each image. In this figure, the peak spot intensity is plotted versus exposure time, and colored data corresponds to the imaging angle. The maximum y-value bound for these plots is 255 to denote the saturated pixel value for 8-bit imaging, used here. Note that the 0° data for LHS-1 is omitted due to an error in the image acquisition, and that the exposure values for the subplots differ. For all materials, the peak spot intensities increase with increasing exposure time, and also when imaging at more normal angles relative to the laser grid projection. The increasing trend with exposure is linear at lower exposure values for each angle, but flattens at higher exposure values. This is partially due to the averaging of the peak spot intensities over a finite number of grid dots, and not because the camera becomes non-linear at these higher exposures.

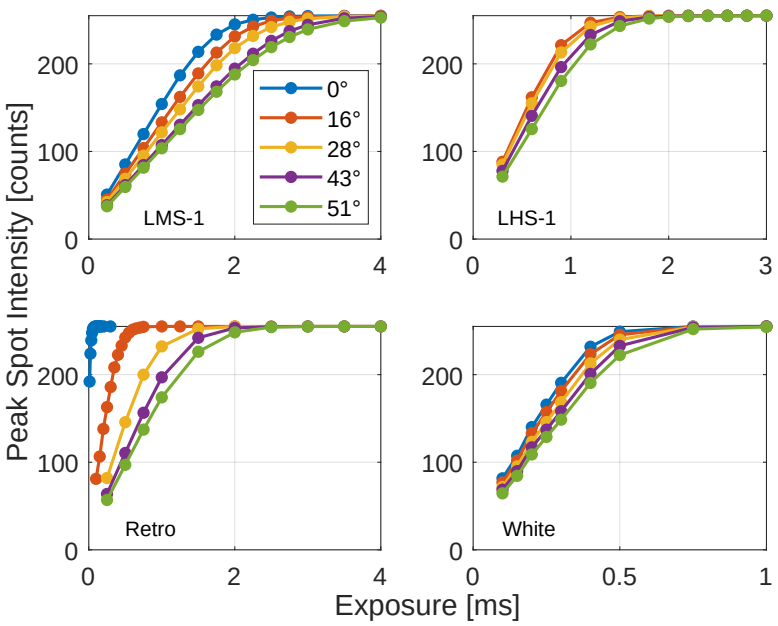

Fig. 5 Peak spot intensity versus exposure and angle for four target materials: LMS-1, LHS-1, Retro, and White. Maximum y-value of the plots corresponds to the 8-bit image saturation limit of 255.

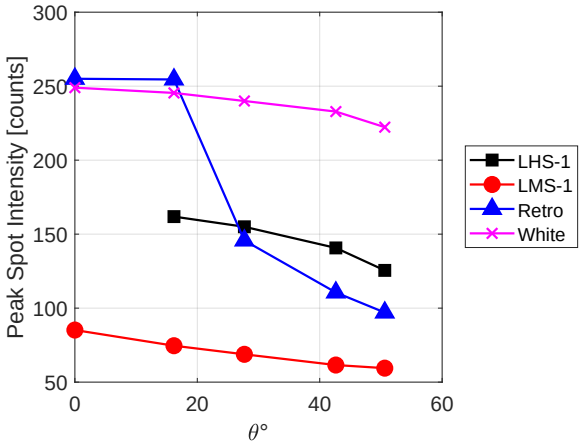

Fig. 6 Peak spot intensity versus imaging angle θ for four materials at an exposure of 500 μs.

When comparing the LMS-1 data to all other materials in Fig. 6, it is clear that it has the weakest intensity return to the camera, since a longer exposure is required to achieve the same counts as other materials at the same imaging angle. The LHS-1 simulant appears to be approximately a factor of two better at scattering light than the LMS-1, demonstrating that landing at lunar locations that have different regolith optical properties will change the design/settings of the imaging system. The white foam board is a further factor of two better than the LHS-1 simulant at scattering the incident laser light. The LHS-1, LMS-1, and white foam board all behave approximately the same with respect to imaging angle changes, where the smaller the imaging angle relative to the light projection, the brighter the imaged dot intensities are, with a consistent increase in this intensity with decrease in angle (albeit with a relatively small factor of ≈ 2). For the retroreflective material, however, a different trend is observed with angle change. At very large imaging angles (51°), the imaged intensity is low, although still better than the LMS-1. As the imaging angle decreases, the imaged intensity quickly increases such that at 16°, the saturation of the dots occurs near 1.5 ms exposure, approximately the same value

as the 0° saturation exposure for the white foam board, and at 0°, the imaged dots saturate almost immediately, near the lowest possible exposure time of the camera (10 μs). This is to be expected, since retroreflective material is designed to have the highest intensity return at the same incidence angle of the illumination. These trends can also be seen in the plot of peak spot intensities versus imaging angle for the four materials shown in Fig. 6, where data for each material and imaging angle was extracted at an exposure time of 500 μs. The LMS-1 scatters the least amount of light, the LHS-1 an intermediate amount, and the white foam board the most, with the small influence of the imaging angle made visible by the shallow slopes of the data. In constrast, the retroreflective material behaves nonlinearly in its peak spot intensity with imaging angle, drastically increasing to a saturated value below 20°.

The data from this testing can be useful for planning the stereo camera laser grid projection system, including selection of the laser power, laser grid dot number, and camera exposure (although auto-exposure could also be used). The orientation of the cameras relative to the laser grid projection axis dictates the imaging angle for both cameras. A desired peak spot intensity can be selected given a known laser power, and the exposure and number of total grid dots can be adjusted to select the most desired operating characteristics. For example, if a higher density of laser dots is required to provide a finer depth map, the exposure can be increased. However, if a lower exposure is required due to higher velocities of the lander to avoid blurring of the images, then a coarser laser grid pattern can be selected. Adjustments can also be made to the laser power if possible to achieve both a decrease in the exposure and an increase in the number of grid dots. Using the data from the most conservative regolith simulant data tested in this paper, LMS-1, these design decisions can be made, and it can be reasonably expected that any deviations from the reflection/scattering characteristics of the LMS-1 will tend to increase the mean spot intensity, thus not adversely affecting the measurements. Ideally, however, soil samples or simulants with similar optical properties as the landing site would be used for this analysis.

IV. Laser Dot Brightness/Saturation Impact on Depth Map

The testing of Section III will help determine the optimum settings for laser power, DOE grid dot number, and camera parameters, using laser dot intensity imaging information. However, because it is unknown exactly what the lunar regolith optical properties will be, the as-designed intensity of the laser dots in the actual flight images may be different than anticipated. In the event that the system was designed such that the actual images over- or under-expose the regions of the laser dots, testing is conducted here to ensure the laser dots with off-design brightness do not affect the depth map values. A flat plate of acrylic was used as a target for the laser dots, oriented orthogonal to the camera baseline (line connecting the origins of both camera coordinate systems). The room lights were turned off, so the only light in the images was from the laser dots, with the laser power set to 100 mW. Data were taken at three target positions (105 cm, 218 cm, 404 cm), to ensure there were no dependence on how big the laser spot sizes were. The camera exposures were chosen such that the images started at sub-saturation levels and proceeded to extreme saturation values, up to the point where the laser dots were bleeding into each other and no defined borders could be seen.

Figure 7 contains sub-images corresponding to different combinations of target distance and exposure times or gain. The top row (blue) is for the closest position of the target, the top-middle row (red) is for the middle position of the target, and the bottom-middle row (yellow) is for the farthest position of the target. Each sub-image in these three top rows corresponds to a camera exposure time, as indicated directly above the sub-image, where the sub-image field-of-view encompasses a single laser dot fully and extends to the adjacent neighboring dots in each direction to show the effect of pixel intensity bleeding at higher exposures. The bottom row (green) is for a close/middle position of the target, but instead of changing the camera exposure, the camera gain is changed, again indicated directly above each sub-image, and an exposure of 1 ms was used for all images. Note that a gain of 0 dB was used for all data in this paper except this one data set. The color-highlighted sub-image in each row denotes the image used as the "truth" for the computation of the mean percent difference.

Unlike the single-camera data processing of Section III, the stereo imaging system was used for testing here. For each target position and exposure/gain, the stereo camera calibration was used to rectify the images, and an in-house processing code was used to compute a depth map for the 17×17 laser dot grid [15]. For each exposure in a target-position test, the percent difference between the depth at that exposure and the depth of the reference exposure were computed, and then an average of the absolute value of all these percent differences was computed. The absolute value ensures that positive and negative depth differences do not cancel each other out. For each exposure, a single mean percent difference value is computed, and for the reference exposure, this value is by definition equal to zero.

The mean percent difference versus camera exposure is plotted in Fig. 8a for the three target positions (near, middle,

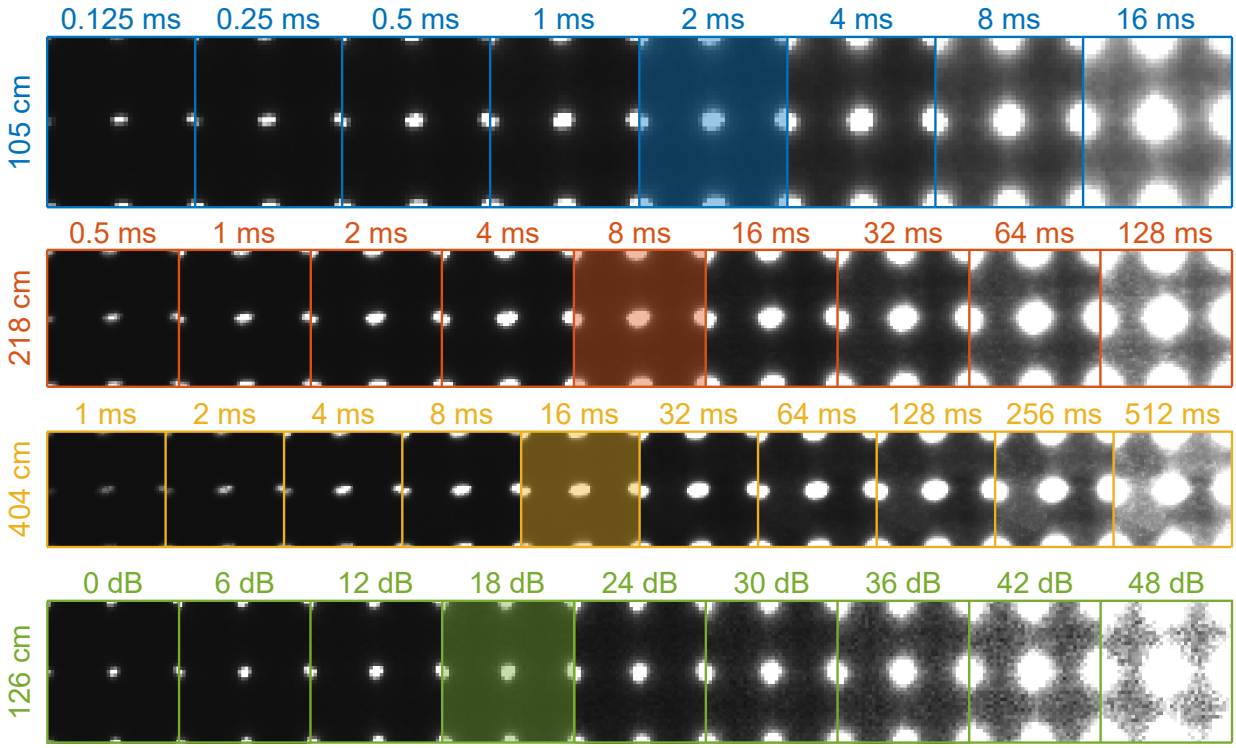

Fig. 7 Images of laser dot intensities for various target positions (rows), camera exposures (blue, red, yellow), and gain (green). Exposures and gain are indicated directly above their respective sub-images. A gain of 0 dB was used for exposure testing, and an exposure of 1 ms was used for gain testing.

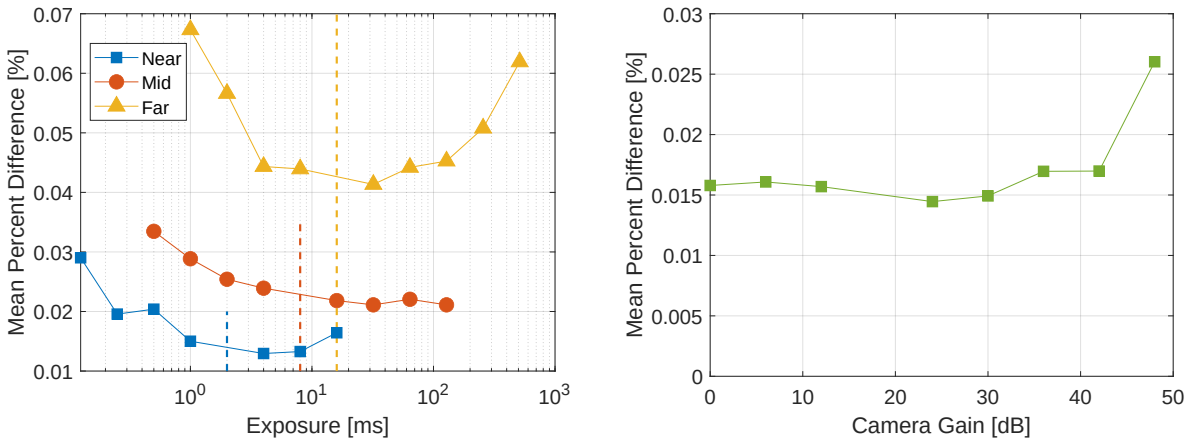

(a) **(b)**

Fig. 8 Mean percent different plotted (a) versus camera exposure for three target positions (near, middle, far) at a camera gain of 0 dB, and (b) versus camera gain at camera exposure of 1 ms. Colors correspond to Fig. 7.

far), with colors corresponding to the images in Fig. 7. The exposure is plotted on a log scale, and the reference exposure for each target position (color-shaded regions in Fig. 7) are indicated by a vertical dashed line. Note that the marker for each data set at the reference exposure is not shown since its position would be at zero on the y-axis. The mean percent difference generally increases as the target position is moved farther from the cameras, possibly due to the

smaller dot sizes in the images at the longer distances. For each target position, the lower exposures have larger mean percent differences, and for the near and far target positions, as the exposure increases, the mean percent difference also increases. This is clearest for the far target position, where any decrease or increase of the exposure from the reference exposure value increases the mean percent difference. While there are definite increases in the mean percent differences with exposures outside the "optimal" reference range, the magnitudes of all the data presented in this plot are small, less than 0.1%. Similar results are seen in the mean percent difference plotted versus increasing camera gain in Fig. 8b, where up to approximately 30 dB, the gain seems to have little impact on the mean percent difference, and even at the higher gain values, the magnitudes of these values are again below 0.1%. These results indicate that a wide range of laser dot intensities (over roughly two decades of exposure times) can be imaged while still retaining high quality depth map reconstructions. Note, however, that the largest target distance that was able to be tested is still smaller than some landing altitudes of lunar landers, and further testing is required at these larger distances to ensure the mean percent difference remains below an acceptable value. While low and high laser dot intensities appear to have little impact on these reconstructions, it is generally good practice to design the system to keep the intensities roughly near the half-dynamic-range of the camera system, although this may not be the case when using a purely binarization-based region identification algorithm with laser dots that are non-uniform in their intensity.

V. Angled Target Measurement

During the PSI process, there is a possibility of deep craters being formed with steep edges. This is expected for the Artemis-class landers which are significantly larger than the Apollo-class landers, and will induce different regimes of deep cratering unlike the shallow, diffuse cratering seen during Apollo missions. With large stereo camera separation distances, these crater edges can become close to parallel with a camera's imaging axis. Even with laser dots adequately displayed onto the entire crater and edges, if the crater edge is aligned with the camera imaging axis, measurements of the depth of those obscured regions may not be possible. To evaluate the stereo system's ability to accurately determine the depth when one camera has a near-glancing view of the laser dots, a series of tests using a flat piece of acrylic as a target board were performed. This target was mounted on a tripod at three positions away from the cameras, roughly 65 cm, 145 cm, and 400 cm, as shown in the top-view schematic of Fig. 9. At each of these positions, five rotation angles of the target board were used. Two of these angles corresponded to extreme angles for one camera or the other (blue, green), one was for a view equally spaced between the cameras (yellow), and two were for shallower angled views (red, purple), for a total of 15 images. The laser power was set to 25 mW, the camera exposure was 70 ms, and the gain was 0 dB.

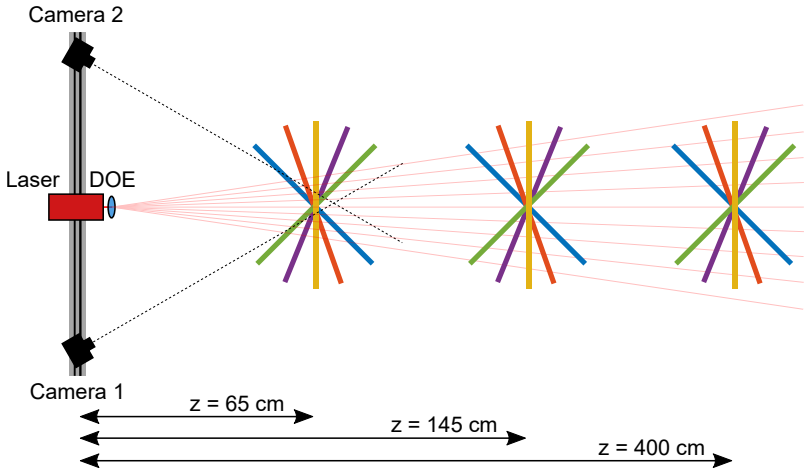

Fig. 9 Top-view schematic of the angled flat target measurements, with three target distances and five rotation angles at each target distance.

For each dataset, the stereo images from both cameras were processed to compute the depth map at each laser dot position. For the near target position, all 289 laser dots were incident on the target board, which has a dimension of 48×33 cm. At the middle target position, 178 dots were incident on the board, and at the far target position, only 15

dots were incident on the board. This is due to the diverging grid pattern, resulting in fewer dots on the target board of fixed size as the distance from the laser/DOE increases. Top-down views of the computed depth maps for each target distance and all target angles are shown in Fig. 10, where (a) corresponds to the near target position at z = 65 cm, (b) corresponds to the middle target position at z = 145 cm, and (c) corresponds to the far target position at z = 400 cm, with colors corresponding to those of Fig. 9. For each target distance, the yellow board positions appear very nearly orthogonal to the laser projection axis. The z positions indicated on the schematic and the bottom of each figure in Fig. 10, measured using a tape measure, closely match the depth value computed for the yellow board position. As the distance of the target away from the cameras increased, so did the maximum angle at which the extremely angled target could be rotated while still retaining separation of the laser dots in the images (blue, green). The angled boards do not all rotate about a central axis because the target needed to be repositioned slightly after every rotation to ensure the same laser dots were incident on the target for every angle. This was done to ensure one-to-one comparison of the depth maps for every rotation angle.

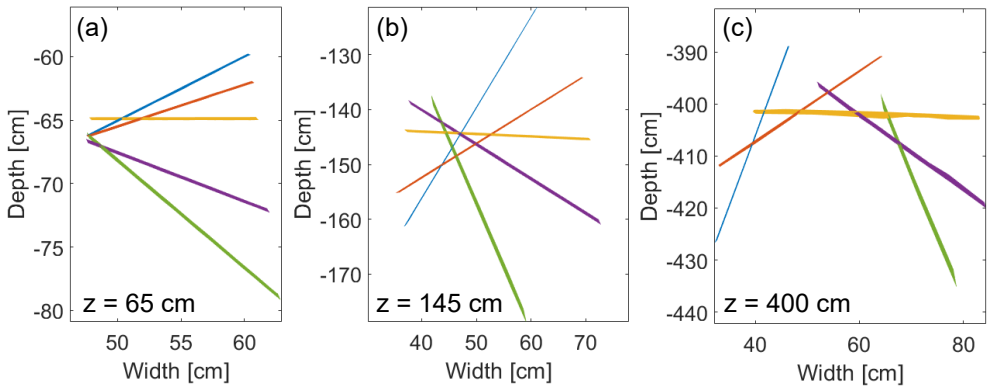

Fig. 10 Angled target top-view of computed depth maps for all five angles at three board positions: (a) near, 65 cm**, (b) middle,** 145 cm**, and (c) far,** 400 cm**.**

For each depth map computed at each target distance/angle, a dot-by-dot depth difference was computed relative to the yellow target for that target distance, to be used as an error metric. For example, at the z = 65 cm target distance shown in Fig. 10(a), dot-by-dot depth differences (for all 289 dots) were computed for the blue, red, purple, and green target angles, all relative to the yellow target angle. Note that the dot position on the target itself changes with rotation angle, and so it is assumed that the target board is flat for these calculations. However, any deviations in flatness of the target board will contribute to the depth differences calculated.

In Fig. 11a, histograms of the depth differences are shown for each target angle, with the yellow target angle ($\approx 0°$) excluded because the depth differences are zero by definition. The top row (black) is for the near target position at z = 65 cm, the middle row (red) for the middle target position at 145 cm, and the bottom row for the far target position at z = 400 cm. The angles indicated above each histogram were computed from normal vectors of the depth map planes. For each row of histograms, the x-axis bounds remain the same, but are different between rows. These histogram plots show the small depth differences for the near target positions, while at the middle and far target positions, the depth differences become larger. However, the most extreme target angles for the near position are close to those of the intermediate angles of the middle position ($-40°$ vs. $-35°$, and $27°$ vs. $30°$). After taking the average of the absolute value of all depth differences and plotting this value against the target angle from the orthogonal, as shown in Fig. 11b, it can be seen that the mean depth differences for these comparable angles at the near and middle target positions are approximately the same, at 0.5 mm (red and black data between $-50°$ and $50°$). As the target angles increase in both directions for the middle and far target distances, the mean depth difference also increases, approximately the same amount for positive and negative angles as would be expected. Because the mean depth difference calculation includes an absolute value of the depth differences over all laser dots, any skew towards negative or positives angles is lost, but when looking at the middle and far target distances of the histogram at the most extreme angles, there appears to be a skew towards a larger number of negative depth differences for negative target angles, and more positive depth differences for positive target angles. Extreme viewing angles will cause an increase in the error of the measurement as shown in Fig. 11b, and the maximum value of $\approx$ 3.3 mm is on the same order as the desired measurement resolution of the CLPS lander mission, so care must be taken when interpreting depth map data from regions of extreme imaging

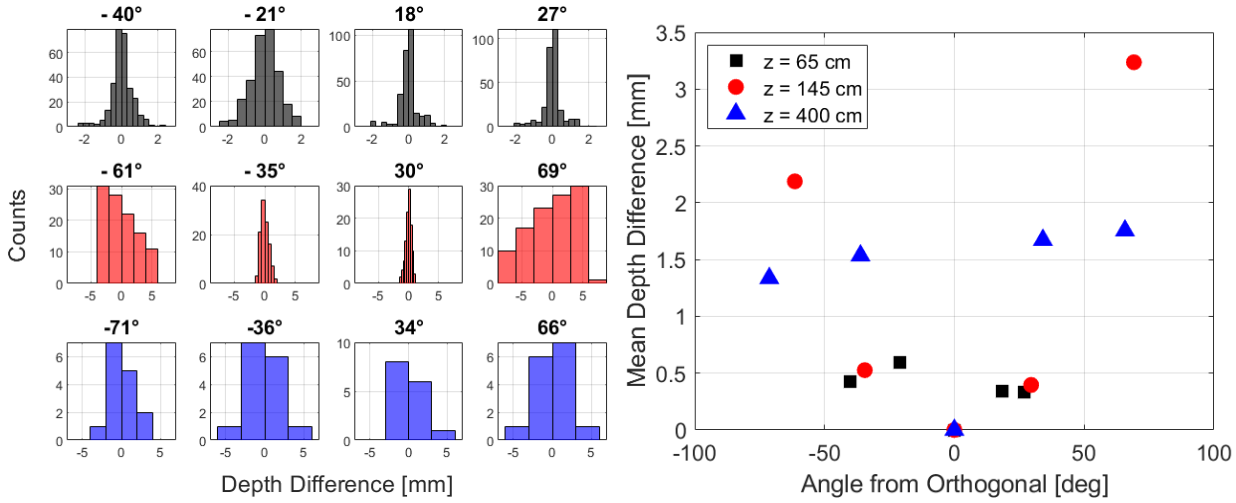

(a) **(b)**

Fig. 11 (a) Histogram of depth differences for each laser dot for the (top row) near z = 65 cm, (middle row) middle z = 145 cm, and (bottom row) far z = 400 cm target positions for each target angle. (b) Mean depth difference of all laser dots for three target positions at all target angles, referenced to the yellow target orientation (0°).

angle relative to one or more cameras.

VI. Ejecta Sheet Measurement

When a rocket plume impinges on the lunar surface, it interacts with the surface in such a way to cause regolith and rocks to be ejected at high speeds radially outward from the crater, which has the potential to damage the lander and/or existing equipment/structures [18]. In addition to making measurements of the crater shape before, during, and after landing, the laser projection system has the ability to measure the extent of this so-called "ejecta sheet". Light from the laser beam will scatter and reflect off the regolith ejected from the crater, and when this scattering is visible in both camera images, the position of the scattering, and thus the ejecta sheet, can be determined. This measurement can be considered a secondary objective to the primary goal of crater depth map measurements, and may provide useful insights for computer simulations that model this fluid/particle PSI flow. Such measurements would provide useful data even during total obscuration that may occur during lunar landings.

A. Ejecta Sheet Field-of-View

A depth map can be computed for any location in space where the field-of-view of the two stereo cameras overlap, as depicted in the schematic of Fig. 12, where the camera 1 field-of-view is shown in green, the camera 2 field-of-view in blue, and the stereo overlap region in gray. If landing in a location where there is no external sunlight illumination, however, the only locations where depth values can be computed are from the laser grid dots as they project from the laser/DOE through the ejecta sheet and eventually to the ground. To demonstrate the bounds of the achievable ejecta sheet limits at various distances from the camera/laser/DOE system, a flat board target was placed orthogonal to the laser grid projection axis at eight locations as shown in the top-view schematic of Fig. 12. The closest position (1) was chosen such that only a small portion of the entire laser grid was visible by both cameras.

For each target position, an image was taken by both cameras and the depth map was computed using the stereo camera calibration, for a total of eight depth maps. In Figs. 13a and 13b, all raw (not yet rectified) image acquisitions were combined into a single image for camera 1 and camera 2, respectively. These images are cropped to a smaller region encompassing only the target at positions 1 through 8, since the images are quite large when using 5.4 mm lenses.

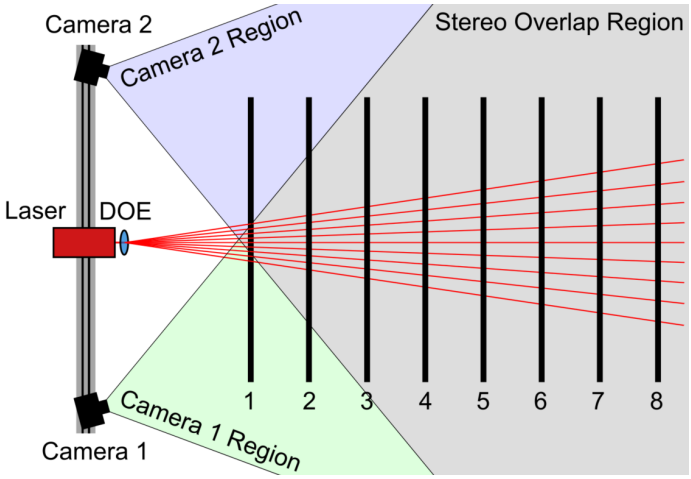

Fig. 12 Top-view schematic of the static ejecta sheet field-of-view testing, with camera 1 field-of-view in green, camera 2 field-of-view in blue, the stereo overlap region in gray, and eight target board positions labeled.

In these images, the laser grid is seen expanding away from the cameras (from the left in Fig. 13a and from the right in Fig. 13b) as the distance increases. The first (closest) image of the grid only has a few laser dots visible in both cameras, and demonstrates the close limit of the ejecta sheet reconstruction capability.

The depth maps computed from each target board position are shown plotted in Fig. 13c, where again, the increasing distance away from from the cameras is accompanied by an increasing laser grid size due to the divergence of the laser grid. Solid black lines are plotted between the four corners of the closest and farthest full grids (excluding the grid at position 1). These lines pass through the corners of the intermediate grid positions, verifying the linear increase in size of the grid with distance as expected, and denote the limits of the measurable ejecta sheet. If a wider divergence angle DOE were selected, this measured ejecta sheet region would be larger, but for the same number of grid points, would have less resolution.

The testing performed in this section is similar to that of the divergence angle calculation of Section II. The DOE used for all testing in this paper, DE-R-206, is a 17×17 grid with a design divergence angle of 15.2° at a design wavelength of 660 nm. In the earlier section, the divergence angle was measured as 14.9° at 638 nm. From the data outlined in this section, the divergence angle of the pattern was calculated to be 14.6°, roughly matching the design and measured values from earlier. Although testing was performed in this section to show the ejecta sheet field-of-view extents, this can be easily simulated in CAD for a particular DOE and camera geometry.

B. Transient PSI Measurements

The testing of Section VI.A demonstrated the static ejecta sheet field-of-view limitations, but the ability of the camera and laser grid system to measure a transient PSI event still needed to be demonstrated. Preliminary proof-of-concept ejecta sheet measurement images were presented in Fig. 15 of Ref. [14], but a depth map was not computed because the images were taken with a single external camera instead of the stereo camera system. The same transient PSI enclosure used in Ref. [14] was used for the measurements in this section, with slight modifications in order to test the dynamic interaction of a gas jet with the lunar regolith simulant. This enclosure (58 cm $\times$ 43 cm $\times$ 33 cm) was constructed with clear acrylic sides and a clear acrylic lid in which a small hose and 3.2 mm diameter needle nozzle were mounted to simulate a rocket plume, with the nozzle placed roughly 10 cm above the simulant particle bed, as shown in the front and side schematics of Fig. 14a. This hose was connected to a compressed air supply where pressure could be regulated with a ball valve. A mirror with nearly the same width as the enclosure was mounted at approximately 45° relative to the enclosure lid to reflect the imaging path and laser/DOE grid projection. The enclosure was mounted inside a fume hood to contain any lunar simulant that escaped the enclosure as these particles pose a breathing hazard. Lab coats, gloves, respirators, and goggles were used when handling the lunar regolith simulant to avoid contact with, and ingestion of, the particles. The cameras and laser grid were located outside the fume hood, imaging horizontally through the fume hood window, reflecting off the 45° mirror, and imaging the regolith bed from above. The image of Fig. 14b shows a cell

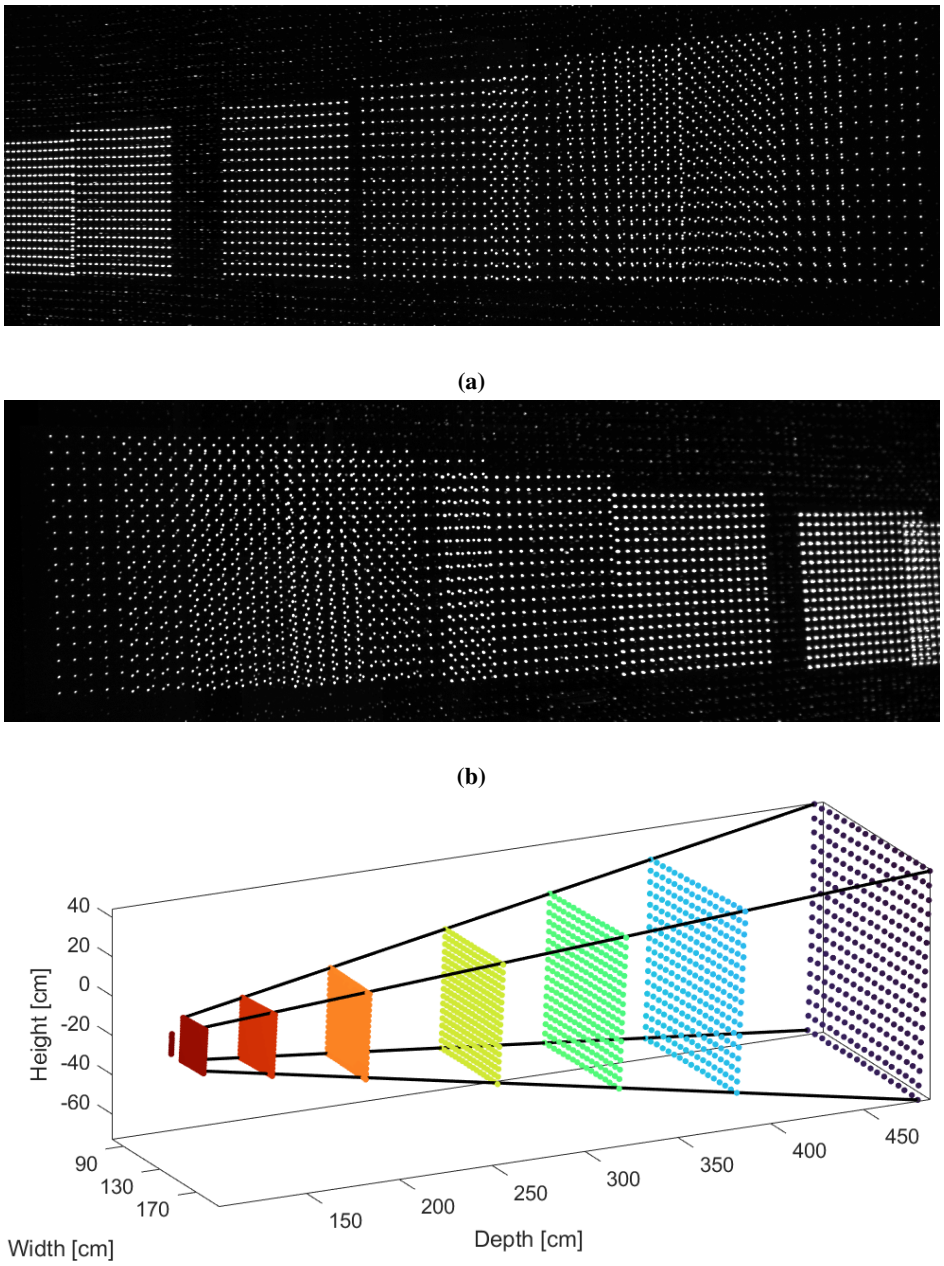

Fig. 13 Cropped raw images of eight image acquisitions of the laser-dot grid at various distances from (a) camera 1 and (b) camera 2, and (c) depth map from processed images showing the extents of the potential ejecta sheet measurement.

phone camera image of the enclosure and mirror, where both the top-view from the mirror and the side view through the front window show the simulant tray.

While this enclosure is a useful test stand for lab testing in small spaces, there are several limitations, where other test facilities will need to be used. First, the enclosure cannot be operated at any pressure other than atmospheric pressure. Second, due to the requirement that the enclosure be located inside a fume hood for particle safety concerns, the enclosure cannot be larger than the interior dimensions of the fume hood itself. Third, because the enclosure is located inside the fume hood and no optical access is available from the top-down, to provide a truly downward viewing

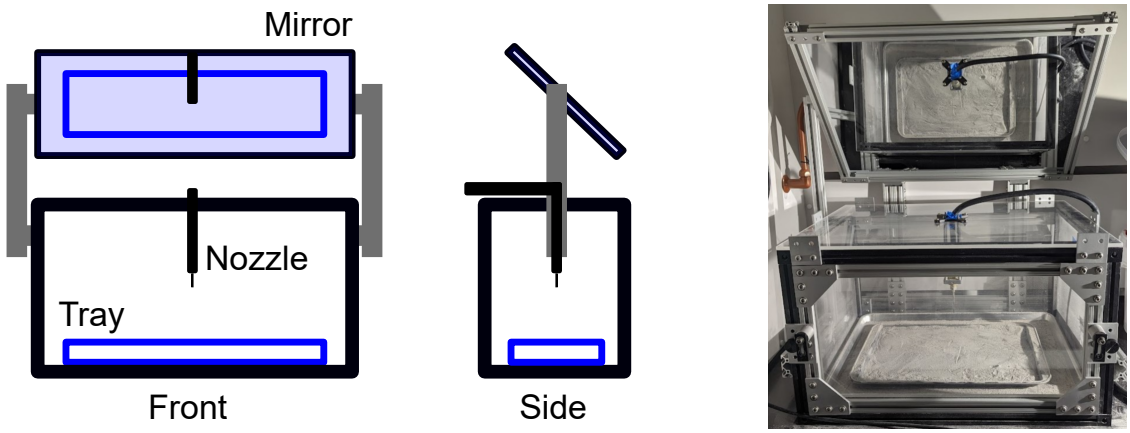

(a) (b)

Fig. 14 PSI enclosure (a) schematic with front and side views, and (b) image showing the combined top-view and side-view of the simulant tray in the enclosure.

orientation of the lasers and cameras, the turning mirror is required, which then also limits the camera and laser positions relative to the mirror and enclosure. The test results discussed in the next subsection merely demonstrate the technology and measurement technique operating within these test limitations. One unexpected benefit of this enclosure with its transparent front window, however, is that simultaneous images of the top view and the side view of the crater and ejecta sheet are visible.

Tests were first conducted without the laser grid illumination, using only a floodlight aimed at the mirror and enclosure to provide illumination, with images from the side window of the enclosure shown in Fig. 15a and images from the top window (after mirror reflection) in Fig. 15b, both only shown for the left camera of the stereo imaging system. The side and top images are both cropped from the same larger image for clarity, where the original image looks similar to that shown in Fig. 14b. Note that the simulant tray does not take up the entire field-of-view of the mirror reflection. A set of eight images are shown, each frame being separated by 50 ms due to the frame rate of the camera of 20 Hz, where 0 ms corresponds to the frame just prior to flow through the nozzle. From the side-view images of Fig. 15a, the particle bed appears to first be ejected laterally close to the bed surface before suddenly being ejected nearly vertically at 200 ms. This progression can also be seen in the top-view images of Fig. 15b, where a clearer view of the initial crater can be seen in the images of 150 ms and 200 ms.

From the stereo image pairs at each time instance of the floodlight testing sequence, a depth map was computed using an automated cross-correlation algorithm, with depth map results plotted in Fig. 15c, where a value of 0 mm denotes the undisturbed simulant bed, and increasing positive depth values denote flow closer to the top of the enclosure, and thus the cameras. The number of points in the depth map depends on the size of the cross-correlation window during processing. Note that the height of the enclosure is 330 mm, and so this is the maximum height that the ejecta sheet can reach. In all depth maps, the regions of the ejecta sheet that are obscured by the nozzle and hose assembly in the images (see Fig. 15b) are absent in the depth map data, since both cameras must see the ejecta sheet to compute a meaningful depth. For the first two frames, no noticeable movement of the simulant is visible, but for the next two frames, the small increase in depth as the simulant is ejected laterally can be seen. As the plume extends farther upward near the center of the image, the depth map of the ejecta sheet can similarly be seen increasing in height. Because there is no active illumination for these images, the depth map should primarily be reconstructing the top of the ejecta sheet, at the point at which the particulate cloud becomes optically dense, and the features can be matched between the two images. Note, however, that the contrast in these images is low using the floodlight illumination, and there is thus a large uncertainty in the reconstructed depth map values of the ejecta sheet.

To obtain lower uncertainties and potentially penetrate farther into the ejecta sheet and possibly to the ground, the laser grid projection system was used. Side-view and top-view images of an image sequence acquired at 25 Hz (40 ms frame separation) are shown in Figs. 16a and 16b, respectively. In Fig. 16a, the laser grid dots on the ground can be seen in the lower half of the image, and some higher-order dots from the DOE pattern can be seen projected onto the back wall of the enclosure through the front window due to the larger divergence area which was not optimized for this

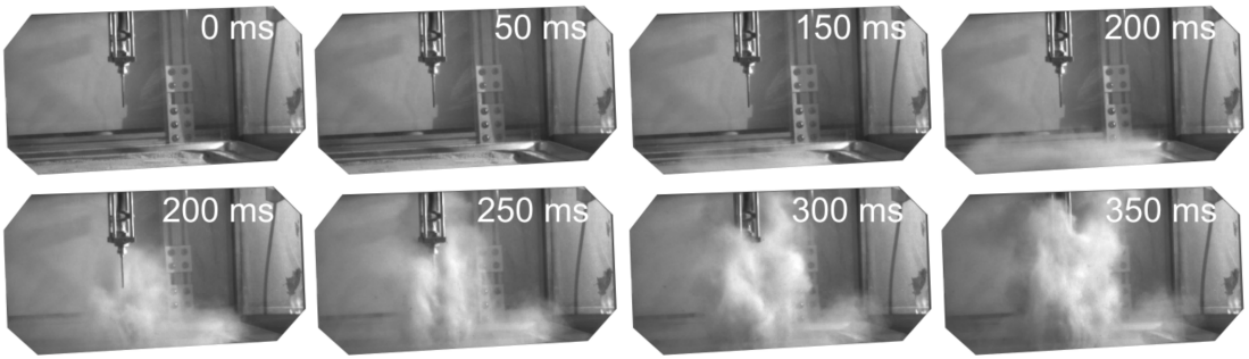

(a)

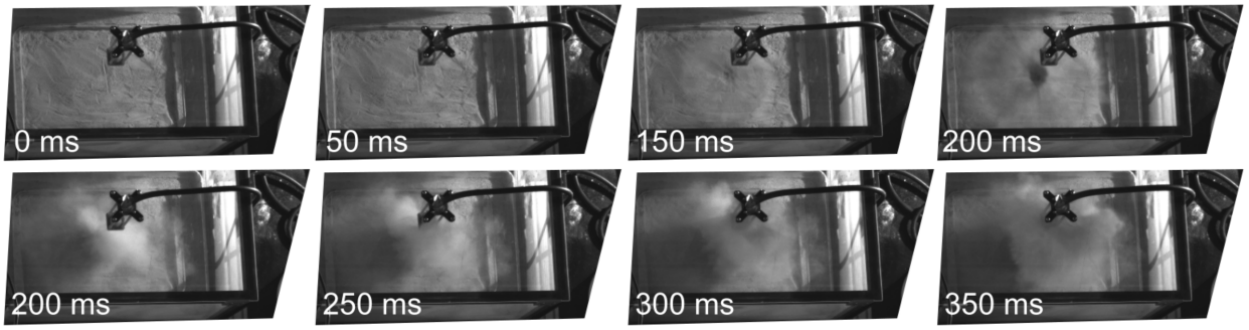

(b)

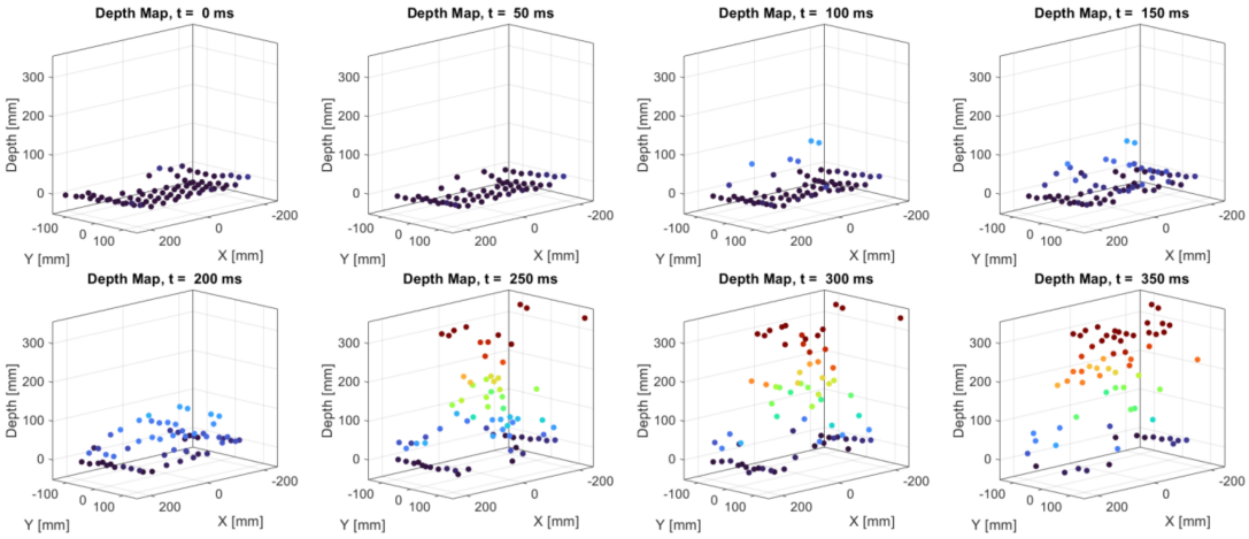

(c)

Fig. 15 Images of the floodlight PSI testing from the (a) side and (b) top views, for selected image frames with times denoted in sub-images. (c) Computed depth maps of the ejecta sheet from each stereo image pair corresponding to images of (b).

PSI enclosure/mirror size. These dots can be ignored as they are not part of the measurement of interest. As with the floodlight testing, the 0 ms frame corresponds to the image just before the nozzle flow was turned on, and immediately after the flow was started, the simulant can be seen increasing in height above the simulant bed, even at 40 ms. From the

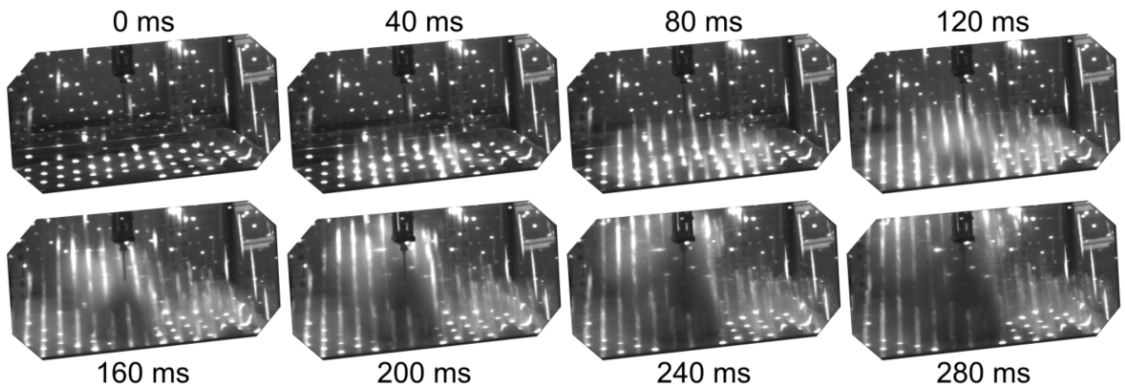

(a)

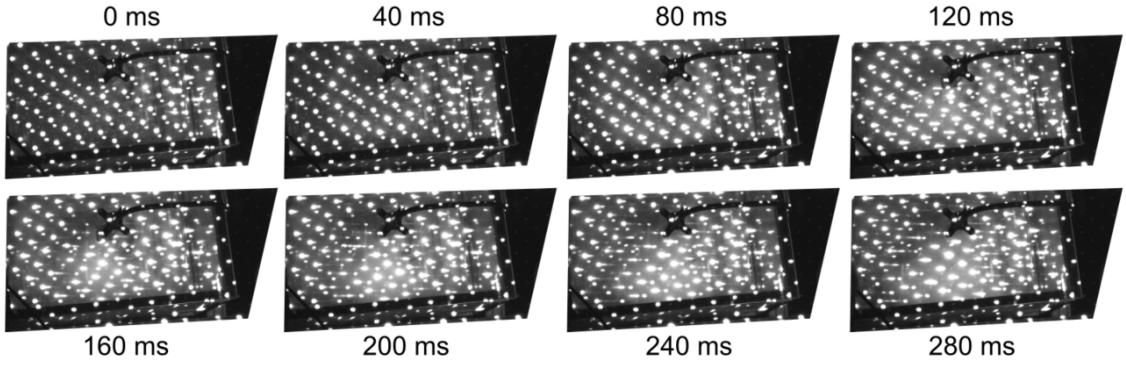

(b)

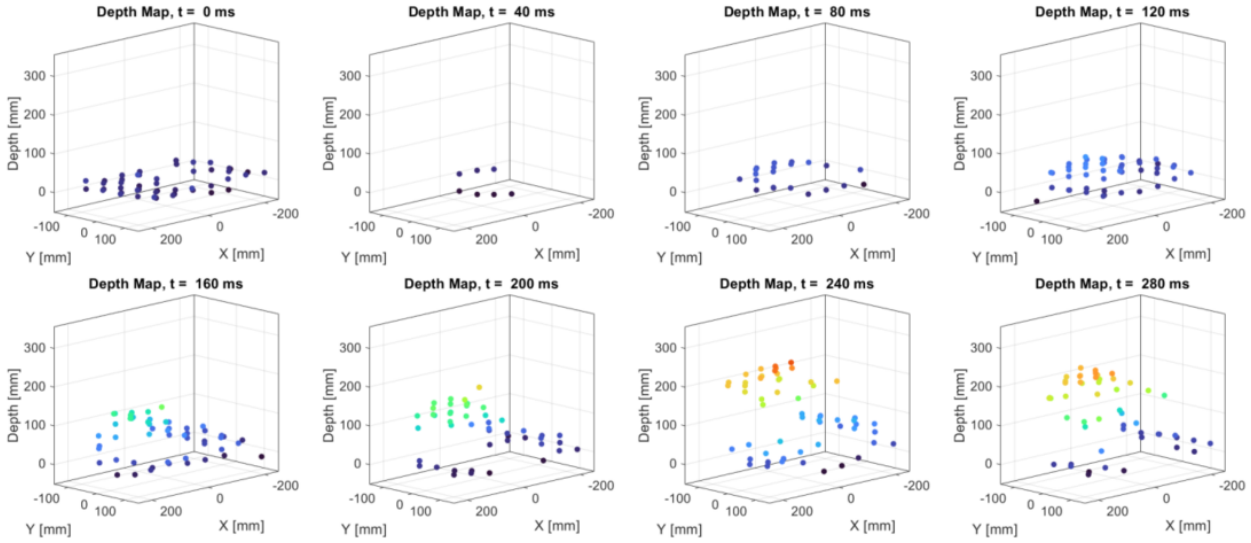

(c)

Fig. 16 Images of the laser grid PSI testing from the (a) side and (b) top views, for selected image frames with times denoted in sub-images. (c) Computed depth maps of the ejecta sheet from each stereo image pair corresponding to images of (b).

side-view images, it is clear that the laser has sufficient power, and the ejecta sheet has insufficient particle density,

such that the laser beams continue to penetrate to the ground. At 280 ms, there is a portion of the ejecta sheet that is optically thick enough to fully attenuate the laser before reaching the ground, but this is isolated to a region close to the nozzle. The top-view images of Fig. 16b are more difficult to evaluate, because for each physical laser beam, there are multiple dots or lines visible in the image. These are due to reflections off the top and bottom surface of the enclosure lid, the scattering from the ejecta sheet, and the scattering of the dots projected on the ground. When the ejecta sheet is not optically thick, the laser penetrates through the sheet thickness, which is then visible in the camera images as a continuous line, as can be seen near the bottom left of the 200 ms image, for example. While these images may make it appear to be difficult to determine laser dot positions and correspondences, when viewing the entire image sequence, it was evident which laser dots corresponded to laser dots in the other camera, and which dots were merely scattering from other surfaces that could be discarded. To remove some of the erroneous scattered laser dots from the images, a flow-off background image was subtracted from the flow-on images, since these erroneous laser grid dots did not move position during the test.

The depth maps from the top-view stereo images of Fig. 16b were computed on a point-by-point basis, instead of the windowed cross-correlation method for the floodlight testing. This allowed for a more precise depth map to be obtained for the ejecta sheet, but where the resolution was then limited by the number of laser dots in the grid pattern reflecting off the mirror and into the enclosure. The depth maps are shown in Fig. 16c, where again a value of 0 mm denotes the undisturbed simulant bed. The same obscuration region seen in the floodlight images is seen in these depth maps since the cameras are in the same locations for both tests, and the laser could not transmit past the nozzle and hose, nor could the cameras view that region. The ejecta sheet can be seen moving upwards in the enclosure with increasing time, and a very clear ejecta sheet boundary is visible, especially for 240 ms and 280 ms. Note that, like the floodlight depth maps, these depth maps also only correspond to the top surface of the ejecta sheet because that was where the dot correspondences were solved for in the processing step. However, in these laser grid images, it is possible to determine the depth/thickness of the ejecta sheet using the penetrating laser lines, and it may also be possible to determine the evolution of the surface crater through an optically thin particle cloud, or with sufficient laser energy in each dot.

C. Optimum DOE Orientation Angle

Two important secondary outcomes of the transient PSI testing of Section VI.B were identified beyond the ability of the system to make measurements of the ejecta sheet. First, the ejecta sheet is not a single thin sheet of minimal thickness, but rather a region or cloud of finite, and sometimes substantial, thickness. Second, the orientation of the laser grid lines scattering within the finite ejecta sheet and imaged on the cameras may make the identification of matching laser dots between camera images difficult. If the DOE is rotated azimuthally in its mount to rotate the projected grid, there will be an optimum orientation of this grid relative to the two cameras that minimizes ambiguity in the laser dot correspondence of the rectified stereo images.

The top-view schematic of Fig. 17 shows a flat target located at two distances away from the camera/laser/DOE system, in the near position at $z = 59$ cm, and at the far position at $z = 110$ cm. Testing at the two positions avoided the need for testing two different grid divergence angle DOEs, since the near position results in a denser grid and the far position results in a coarser grid due to the diverging grid. The target was mounted on a short aluminum rail on top of a tripod, such that the target could be linearly translated away from the laser in the z-direction, a maximum distance of 25 cm. While the target was translated, the cameras were continuously acquiring images at 10 Hz, such that the translation of the target would simulate the ejecta sheet thickness. For both the near and far positions of the target, the DOE was rotated to six angles: 0°, 15°, 30°, 45°, 60°, and 75°.

For each DOE angle at both near and far target positions, images were continuously acquired as the target was manually moved from the front of the rail to the back of the rail, a distance of roughly 25 cm. This movement was made to be as steady as possible, but increases and decreases in the scan speed were inevitable. The image sequences for each DOE angle at both positions were averaged together and contrast-adjusted, and are shown in the images of Fig. 18a and Fig. 18c for the near and far positions, respectively, where the DOE angles are noted in each sub-image, and these sub-images are cropped around the laser grid region for clarity. The same 25 cm translation of the target appears more pronounced for the near images than the far. Only limited information can be extracted from these images, because when there are distinct lines that overlap with adjacent laser dot lines, this makes finding correspondences more difficult because it is not clear where one line ends and another begins. For example, the grid in an orientation of 0° for both near and far positions shows distinct near-horizontal lines, making the selection of the laser dot correspondences difficult. This problem worsens for thicker ejecta sheets, where lines of scatter (instead of points) are observed. In contrast, when the entire region of the pyramidal frustum is filled in, as it is for DOE angles of 15° or 30°, then there may be enough of

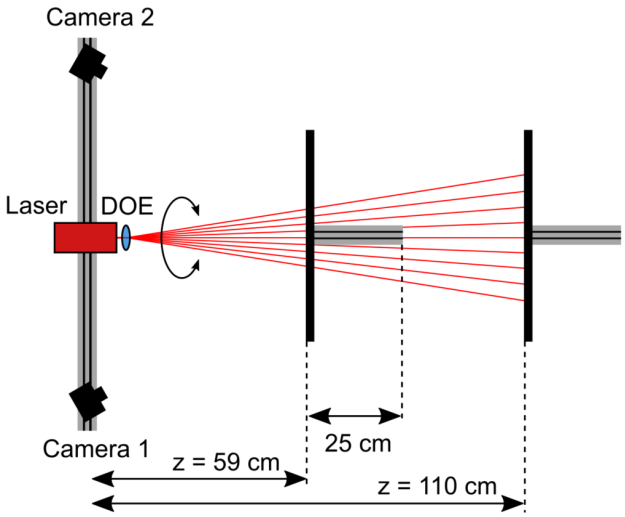

Fig. 17 Top-view schematic of the DOE rotation testing, with two positions of the target board shown (near z = 59 cm, far z = 110 cm), each with a target translation distance of 25 cm to simulate a finite thickness ejecta sheet using continuous image acquisition.

an offset between adjacent laser dots in the vertical direction such that the laser lines can be distinguished from each other. However, this simplified method of identifying the optimum DOE angle is not sufficient.

A different method of identifying the optimum DOE rotation angle can be used, where the image processing method is shown schematically in Fig. 19. For each image sequence for a single DOE angle, a horizontal row of pixels is selected (e.g., a row halfway down the image), and for each frame, this horizontal pixel row is extracted and added as the next row in a new image, where the width of the new image is the width of the original image and the height is the number of frames. The laser dots will appear as bright lines in these frame-slice images, angled down and to the right based on the translation of the target in the camera's field-of-view, as shown in Figs. 18b and 18d for the near and far positions, respectively. Note that the reason these lines are not straight is that the target was moved by hand at a non-constant velocity; had a motorized translation stage been used with constant velocity, these lines would be straight. The separation and density of these lines can provide insight into the ideal DOE angle, where very closely spaced lines result in a measurement that is hard to resolve between laser dots/lines, and more separated lines make this measurement easier. These plots support the earlier qualitative statement that the 0° and 45° DOE orientations are not well suited for ejecta sheet measurements, and that instead one of the intermediate rotation angles should be used, for example, 15°. These plots can also provide a measure of the maximum thickness ejecta sheet that can be measured unambiguously, that is, without lines that overlap, but these calculations are beyond the scope of this paper. Finally, it is possible to use CAD simulations to obtain these measurements and decide on an optimum DOE angle for a given camera configuration [14].

VII. Density Gradient Impact on Depth Map

The final testing performed in this paper concerns the impact that a density gradient may have on the depth map computed when the density gradient impacts one or both cameras or the laser grid projection. This is of concern when imaging directly below a region of strong density gradients, such as those produced by a rocket nozzle plume. A top-view schematic of the density gradient testing is shown in Fig. 20, where a flat plate was used as a target in a near position at 126 cm and a far position at 385 cm, measured from the camera/laser rail. The near position of the target was chosen such that the laser dot grid entirely filled the 48 × 33 cm target, while for the far position, only a subset of the entire laser grid was incident on the target. The laser power was set to 100 mW, the gain to 0 dB, and the camera exposure was 2 ms and 16 ms for the near and far positions, respectively. A heat gun set to its highest temperature setting was used as the strong density object.

Five scenarios are tested, outlined and numbered in the schematic. The first two scenarios test the impact on the depth map when only one camera is affected by the density object, by placing the heat gun in front of either camera 1 (scenario 1) or camera 2 (scenario 2), without affecting the other camera or laser grid projection. The third scenario

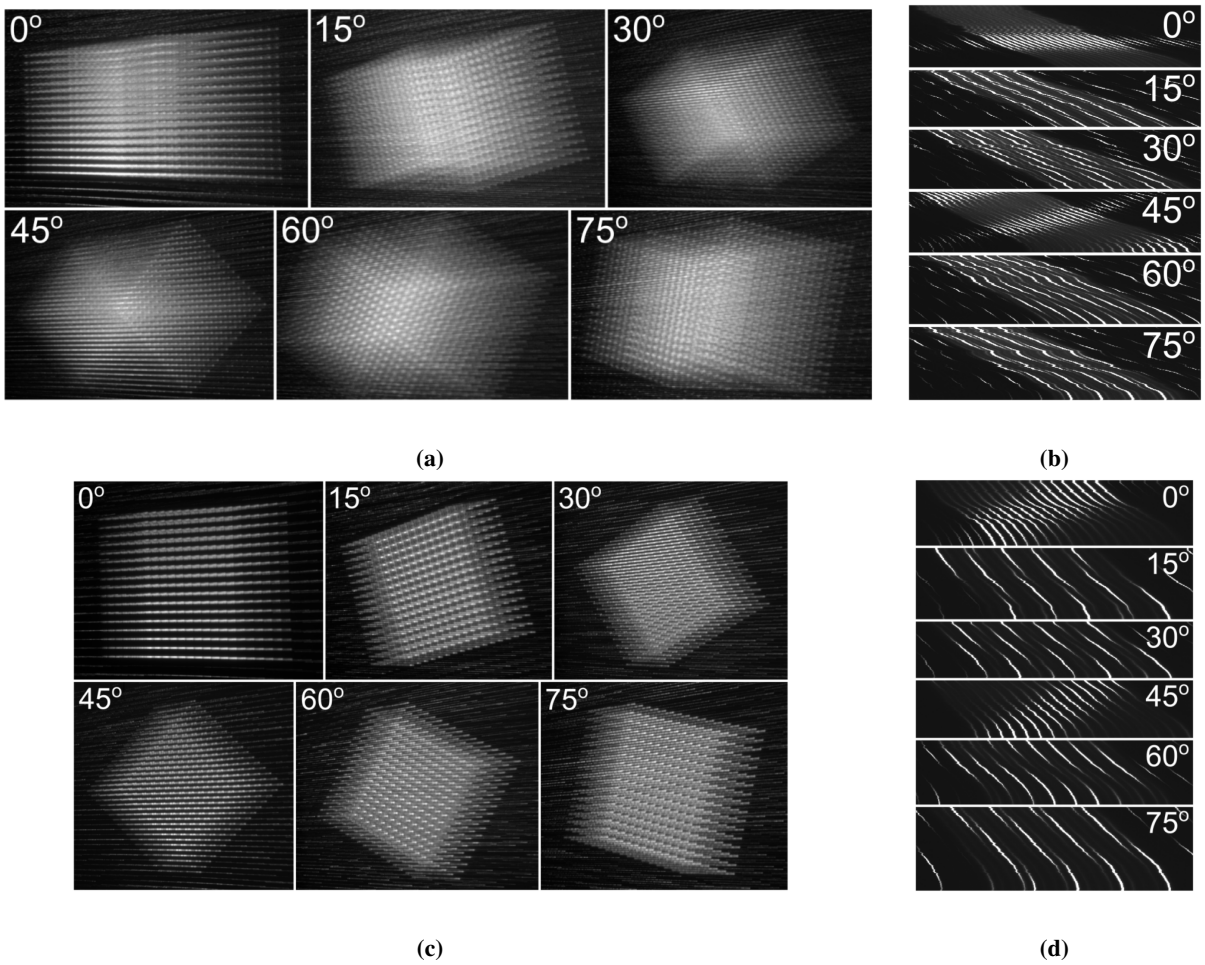

Fig. 18 **(a,c) Averaged images over the 25 cm translation of the target for (a) the near position and (c) the far position. (b,d) Horizontal image slice with increase image slice in the vertical direction for (b) the near position and (c) the far position.**

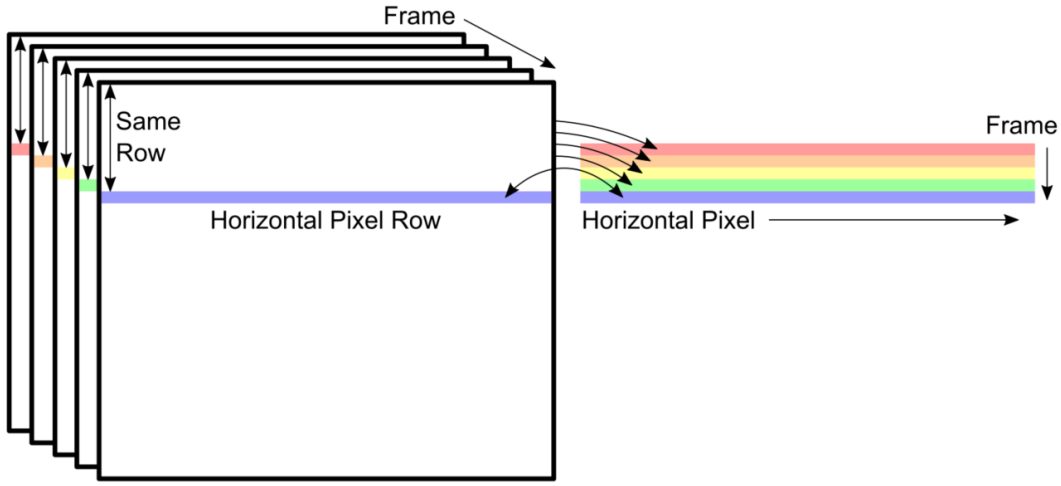

Fig. 19 **Schematic of horizontal slice frame stacking image processing used for results in Fig. 18(b,d).**

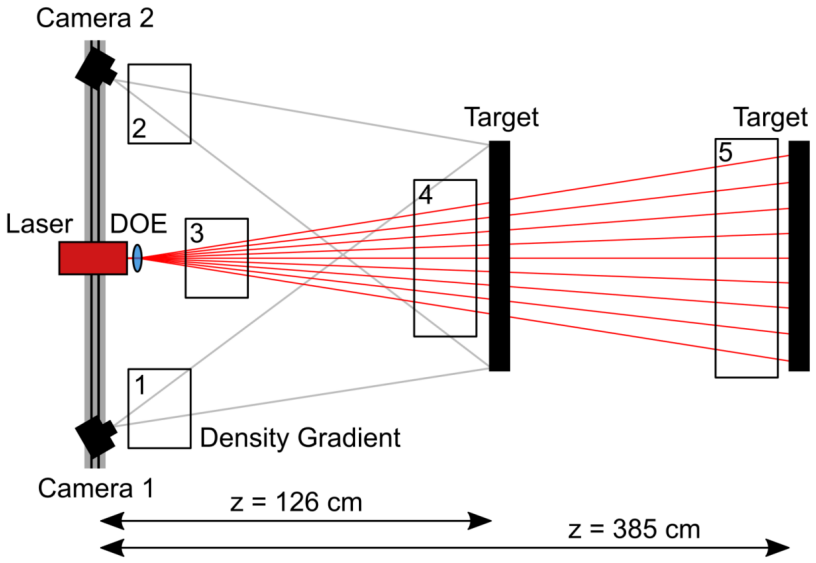

Fig. 20 Top-view schematic of the density gradient testing, with five positions of the heat gun affecting different aspects of the setup.

places the heat gun such that it only affects the projection of the laser grid on the targets, and not the camera's images. The fourth and fifth scenarios place the heat gun directly in front of the target, such that it affects the laser grid projection (very slightly) and both of the camera images simultaneously. For the ground-truth comparison data set, an image was acquired for each scenario without the heat gun.

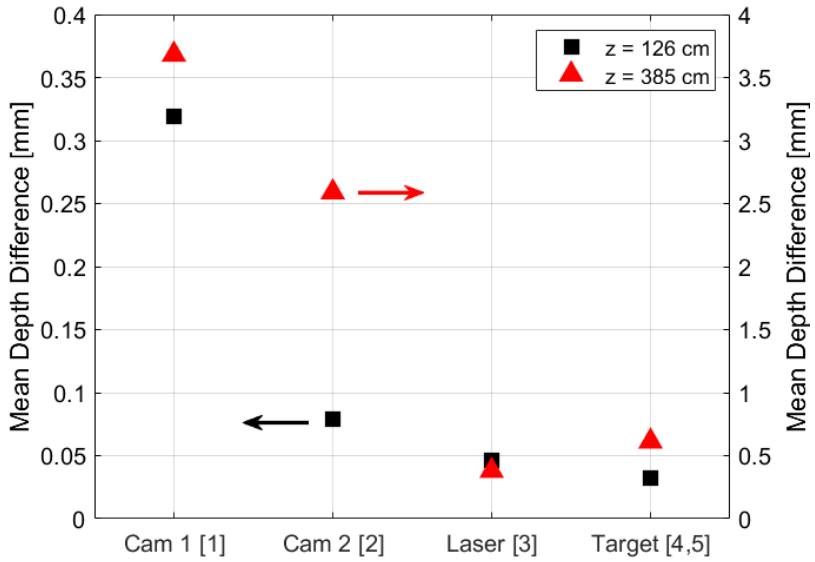

Fig. 21 Mean depth difference for near (126 cm, black, left axis) and far (385 cm, red, right axis) positions, for five testing scenarios indicated on x-axis.

The data were processed similar to previous data sets in this paper, where the depth map was computed for each scenario for both the flow-on and flow-off cases. For each laser dot in the images, the depth difference between the flow-off and flow-on image was computed, and then an average of the absolute value of all these depth differences was computed, resulting in the mean depth difference that is plotted in Fig. 21. Note that only a single flow-on image in the image sequence was used for the results presented here. In this figure, the near target position results are plotted with black squares and correspond to the left axis, while the far target position results are plotted with red triangles and

correspond to the right axis. Note that the right axis is one order of magnitude larger than the left axis. Results are plotted for each scenario for both positions, except scenarios 4 and 5, where data were only acquired for their specific target position (near for 4, far for 5). Interestingly, the mean depth difference between scenarios 1 and 2 are not the same, as might be expected with two identical cameras/lenses. This is likely due to the selection of the frame used for the flow-on/flow-off comparison, where the image with the maximum shift in the laser dots was chosen, but where the scenario 1 images might have been shifted more than those of scenario 2. A better approximation of the mean depth difference can be computed using many images in the image sequence instead of only one. These results nonetheless show that a density gradient affecting only one camera does indeed alter the depth map from its true value, and that this difference is more pronounced at larger imaging distances. For scenario 3, the mean depth difference is minimal for both imaging distances, albeit with a factor of 10 increase for the far target position. This is expected, since although the laser grid may become quite distorted passing through the density object, both cameras view the same pattern on the target, and their images are not distorted relative to each other. Finally, the mean depth differences for scenarios 4 and 5 also show very little impact of the density gradient on the depth maps, indicating that if the density object is not only isolated to one camera, and affects both cameras, the effect may be minimal. One important conclusion drawn from the results in Fig. 21 is that the altitude of the measurement has a large impact on the mean depth difference, and care must be taken to ensure that this distortion does not overshadow the scale of the crater depth itself. Further testing in a more applicable ground test facility can evaluate how a rocket plume might change the results discussed here for a simple heat gun density object. For flight data, computations of this aero-optic distortion effect might be able to be used to provide mean corrections to measurements.

VIII. Conclusions

Testing of an active illumination laser-dot grid-projection system was performed in order to inform the design of both the camera and laser/grid system for an upcoming uncrewed lunar lander mission to the south pole region of the moon. The diffractive optical elements were initially characterized with the intended flight laser system, with results matching the specified parameters from the technical specifications, as expected. Because the laser will be mounted at some distance away from both stereo cameras, the angle between the laser projection axis and the cameras' imaging axes will be some finite value. The effect of both camera exposure and camera imaging angle relative to the grid projection was explored for four target materials, including two lunar regolith simulants, white foam board, and a retroreflective material. The peak laser dot intensities increased as the angle between the camera and the laser decreased for all target materials and both laser powers. Using the most conservative results testing in this paper, the lunar regolith simulant (LMS-1), a laser power, laser dot number, and camera exposure can be selected based on the mission requirements.

To evaluate the effect of decreasing or increasing laser dot brightness on the calculated depth maps, testing was performed with a single laser power and camera exposure times below and above an arbitrarily-defined ideal exposure. For one test, the camera exposure was fixed at the camera gain increased. There was some increase in the mean percent difference of these saturated laser dots from a ground-truth measurement, but these differences were below 0.1% for every tested case for all levels of brightness (including saturation) using both increased/decreased camera exposure and increased camera gain. These results indicate that over nearly two orders of magnitude of camera exposure and laser dot brightness, the calculations of the depth map will not be adversely affected.

The angled board testing verified that even at extreme angles of the laser grid projection on the target (e.g., projection of the grid onto the steep side of a crater), the computed depth maps are reasonably accurate, only deviating from the ground-truth values by less than 4 mm for angles exceeding 70° at the largest distance testing (corresponding to high altitudes). At shorter distances (lower altitudes), the maximum target angles were smaller, limited by the geometry of the stereo camera system used, and results in smaller deviations from the ground-truth values. These tests instilled confidence that as long as both cameras have a view of the laser dots, high-quality depth maps can be computed, and mapping deeper craters or rocks can be accomplished. However, as the angle and imaging distances increase, the depth map differences can be on the same order of magnitude of the desired resolution of the crater depth map itself.

While not a primary objective of the active illumination stereo imaging system for the lunar landing mission, the ability to measure the height and thickness of the ejecta sheet during landing is a welcome secondary benefit of the laser grid illumination system. The PSI enclosure was used to evaluate the feasibility of this ejecta sheet measurement during a transient PSI event, namely a compressed air jet impinging on a bed of lunar regolith simulant. Tracking the height of the ejecta sheet in every subsequent frame of an image sequence was successful, and it was determined that there is an optimal rotation angle of the DOE such that the grid projection results in the least ambiguous selection of corresponding

points in both camera's images.

The density gradient testing demonstrated that with severe density gradients that affected only one camera and not the other, the computed depth maps differed by approximately 3-4 mm from the baseline case where no density gradient was present. While further testing is required for specific imaging cases and potentially with a characteristic rocket nozzle plume in a dedicated ground test, these simple tests assuaged the primary concern that the depth map would be greatly impacted by the cameras imaging through different locations of a density gradient feature. Note again, however, that these depth map differences are on the order of magnitude of the desired resolution of the stereo imaging system, which can pose a problem if the density gradients are more severe than anticipated, and so further ground testing is suggested. The information gathered during testing for this paper will enable more informed design decisions regarding the camera settings, required laser power, and DOE laser dot number and divergence angle.

Acknowledgments

This work was supported by the Stereo Cameras for Lunar Plume-Surface Studies (SCALPSS) Project, which is funded by the NASA Space Technology Mission Directorate (STMD), Game Changing Development (GCD) Program, and the Exploration Systems Development Mission Directorate (ESDMD). The authors would like to thank Brett Bathel, Stephen Jones, and W. Holt Ripley for the assembly of the small-scale PSI enclosure, Mark Kulick for machining capabilities related to the experimental setup, Wesley Chambers for helpful discussions of the characteristics of lunar regolith, and Rostislav "Ross" Kovtun and Ane Slavic from the Simulant Development Lab at NASA Johnson Space Center for providing and arranging the shipment of the lunar regolith simulant. The early development of this work was supported by the NASA CIF/IRAD program under the FY21 project titled "Particle Image Velocimetry/Tracking, Ejecta Sheet Monitoring, and Terrain Mapping for SCALPSS 2". Specific vendor and manufacturer names are explicitly mentioned only to accurately describe the test hardware. The use of vendor and manufacturer names does not imply an endorsement by the U.S. Government, nor does it imply that the specified equipment is the best available.

References

[1] Engle, M., "Operational Considerations for Manned Lunar Landing Missions - Lessons Learned from Apollo," *AIAA Space 2004 Conference and Exhibit*, American Institute of Aeronautics and Astronautics, 2004. doi:10.2514/6.2004-6081.

[2] Gaier, J. R., "The Effects of Lunar Dust on EVA Systems During the Apollo Missions," Tech Report 2005-213610, NASA Glenn Research Center, Mar. 2005.

[3] Metzger, P. T., Lane, J. E., Immer, C. D., and Clements, S., "Cratering and Blowing Soil by Rocket Engines During Lunar Landings," *International Conference on Case Histories in Geotechnical Engineering*, 2008.

[4] Metzger, P. T., Smith, J., and Lane, J. E., "Phenomenology of soil erosion due to rocket exhaust on the Moon and the Mauna Kea lunar test site," *Journal of Geophysical Research*, Vol. 116, No. E6, 2011. doi:10.1029/2010je003745.

[5] Metzger, P. T., "Dust Transport and Its Effect Due to Landing Spacecraft," *The Impact of Lunar Dust on Human Exploration*, LPI Contributions, Vol. 2141, 2020, p. 5040.

[6] Metzger, P. T., "Ejecta Sheet Tracking, Opacity, and Regolith Maturity (Ejecta STORM): An Instrument for Lunar Landing Plume Effects and Dust Dynamics," *52nd Lunar and Planetary Science Conference 2021*, 2021.

[7] Chambers, W. A., "Lighting and the lunar surface environment," *NESC Lunar Lighting Workshop*, 2022.

[8] John, K., Chambers, W., Buhler, C., and Meyer, M., "The Challenge of Lunar Dust," *Unique Science from the Moon in the Artemis Era*, 2022.

[9] Metzger, P. T., Immer, C. D., Donahue, C. M., Vu, B. T., Latta, R. C., and Deyo-Svendsen, M., "Jet-Induced Cratering of a Granular Surface with Application to Lunar Spaceports," *Journal of Aerospace Engineering*, Vol. 22, No. 1, 2009, pp. 24–32. doi:10.1061/(asce)0893-1321(2009)22:1(24).

[10] Gorman, M. T., Rubio, J. S., Diaz-Lopez, M. X., Chambers, W. A., Korzun, A. M., Rabinovitch, J., and Ni, R., "Scaling laws of plume-induced granular cratering," *PNAS Nexus*, Vol. 2, No. 9, 2023. doi:10.1093/pnasnexus/pgad300.

[11] Rodrigues, N. S., Tyrrell, O. K., Danehy, P. M., Eberhart, C. J., McDougal, K. J., Liu, T., Reynolds, T. D., Rubio, J. S., Jiang, N., Hsu, P., and Korzun, A. M., "Flow Visualization for Plume-Surface Interaction Testing Within Large-Scale Vacuum Environments at Conditions Relevant to Lunar and Martian Landers," *JANNAF Exhaust Plume and Signatures Annual Meeting*, 2023.

[12] Thompson, R. J., Danehy, P. M., Munk, M. M., Mehta, M., Manginelli, M. S., Nguyen, C., and Thomas, O. H., "Stereo Camera Simulation for Lunar Surface Photogrammetry," *AIAA SciTech 2021 Forum*, American Institute of Aeronautics and Astronautics, 2021. doi:10.2514/6.2021-0358.

[13] Tyrrell, O. K., Thompson, R. J., Danehy, P. M., Dupuis, C. J., Munk, M. M., Nguyen, C. P., Maddock, R. W., Fahringer, T. W., Krolick, W. C., Weaver, A., West, J., Manginelli, M. S., and Witherow, W. K., "Design of a lunar plume-surface interaction measurement system," *AIAA SciTech 2022 Forum*, American Institute of Aeronautics and Astronautics, 2022. doi:10.2514/6.2022-1693.

[14] Weisberger, J. M., Danehy, P. M., Fahringer, T. W., Bathel, B. F., and Tyrrell, O., "Development of a Terrain Mapping/Crater Evolution Measurement using Diffractive Optical Elements," *AIAA Aviation 2022 Forum*, American Institute of Aeronautics and Astronautics, 2022. doi:10.2514/6.2022-3562.

[15] Tyrrell, O. K., Weisberger, J. M., Fahringer, T. W., Danehy, P. M., and Hutchins, W. D., "Investigating Photogrammetric Accuracy of a Lunar-lander-induced Crater Measurement System," *AIAA SciTech 2023 Forum*, American Institute of Aeronautics and Astronautics, 2023. doi:10.2514/6.2023-2475.

[16] Online, 2023. URL `https://sciences.ucf.edu/class/simulant_lunarhighlands/`.

[17] Online, 2023. URL `https://sciences.ucf.edu/class/simulant_lunarmare/`.

[18] Lane, J. E., and Metzger, P. T., "Estimation of Apollo Lunar Dust Transport using Optical Extinction Measurements," *Acta Geophysica*, Vol. 63, No. 2, 2015, pp. 568–599. doi:10.1515/acgeo-2015-0005.